The effect of reduction treatment in a high-temperature (600 °C) hydrogen-containing environment on the microstructure and tendency to brittle fracture of YSZ–NiO(Ni) materials for solid oxide fuel cell anodes has been studied. To assess the crack growth resistance of the ceramics, the Vickers indentation technique was adapted, which allowed estimating the microhardness and fracture toughness of the material in the complex.

The requirements for high porosity of the anodes to ensure functional properties show that the strength may be an insufficient characteristic of the bearing capacity of the anode. More structurally sensitive characteristics are needed to assess its crack growth resistance.

The average levels of microhardness of YSZ–NiO ceramics in the as-sintered state and YSZ–NiO(Ni) cermets (2.0 GPa and 0.8 GPa, respectively) and their fracture toughness (3.75 MPa·m$^{1/2}$ and 2.9 MPa·m$^{1/2}$, respectively) were experimentally determined.

It was found that the microstructure of YSZ–NiO(Ni) cermet after redox treatment is formed by a YSZ ceramic skeleton with refined Ni-phase grains combined in a network, which provides increased electrical conductivity. Along with higher porosity of the cermet, its fracture toughness is not lower than that of the one-time reduced cermet due to the implementation of the bridging toughening mechanism of fracture.

The proposed treatment method allowed forming the microstructure of the anode material, resistant to crack propagation under mechanical load. The propensity of the anode material to brittle fracture on the basis of evaluation of its crack growth resistance and analysis of the microstructure and fracture micromechanism was substantiated. This result is interesting from a theoretical point of view. From a practical point of view, the developed technique allows determining the conditions of redox treatment in the technology of manufacturing fuel cell anodes

Keywords: YSZ–NiO ceramics, redox treatment, indentation, fracture toughness, fracture mechanism

UDC 539.4.015: 666.3
DOI: 10.15587/1729-4061.2020.218291

ESTIMATION OF THE EFFECT OF REDOX TREATMENT ON MICROSTRUCTURE AND TENDENCY TO BRITTLE FRACTURE OF ANODE MATERIALS OF YSZ–NiO(Ni) SYSTEM

B. Vasyliv
PhD, Senior Researcher
Department of Hydrogen Technologies and Materials of Alternative Power Engineering
Karpenko Physico-Mechanical Institute of the NAS of Ukraine
Naukova str., 5, Lviv, Ukraine, 79060
E-mail: mechengin1111@gmail.com

V. Kulyk
Doctor of Technical Sciences*
E-mail: kulykvolodymyrvolodymyrovych@gmail.com

Z. Duriagina
Doctor of Technical Sciences, Professor*
Doctor Habilitatus, Professor
Institute of Materials Engineering
The John Paul II Catholic University of Lublin
Rac awickie al., 14, Lublin, Poland, 20-950
E-mail: zduriagina@ukr.net

D. Mierzwinski
PhD
Faculty of Material Engineering and Physics
Cracow University of Technology
Warszawska str., 24, Cracow, Poland, 31-155
E-mail: dariusz.mierzwinski@pk.edu.pl

T. Kovbasiuk
PhD*
E-mail: felcproject@gmail.com

T. Tepla
PhD, Associate Professor*
E-mail: tetiana.l.tepla@lpnu.ua

*Department of Applied Materials Science and Materials Engineering
Lviv Polytechnic National University
Bandery str., 12, Lviv, Ukraine, 79013

Received date 10.10.2020
Accepted date 25.11.2020
Published date 22.12.2020

1. Introduction

The strategy of the world's leading states is the intensive development of alternative energy. An important place in this direction is occupied by environmentally friendly technologies of fuel cells, which are electrochemical devices for the direct conversion of chemical energy into electricity. Solid oxide fuel cells (SOFCs) are favor-

ably distinguished among a variety of fuel cell types in terms of efficiency.

In SOFCs, where hydrogen-containing gas mixtures are used as fuel, the most common material for anodes is YSZ–Ni cermet based on zirconium oxide stabilized with yttrium oxide. This material is characterized by high catalytic activity during hydrogen oxidation, structural stability during operation in a hydrogen-containing atmosphere, and a coefficient of thermal expansion close to ZrO_2-based electrolytes [1]. Additive technologies, given their increasing use in powder metallurgy, are considered as a promising tool for the manufacture of SOFC anodes.

Reduction of NiO to Ni is the final stage of processing sintered YSZ–NiO anodes. In our previous works, the results of the study of the YSZ–NiO anode material [2, 3], treated by reduction-oxidation (redox) cycling for 5 cycles with a final one-time reduction, were presented. Based on these researches and the obtained characteristics of strength and electrical conductivity, it was found that the formed cermet has an advantage in strength over the one-time reduced within 4 h material. Besides, the cermet after redox treatment has an electrical conductivity advantage of 2.6 times.

Therefore, at present, the industrial implementation of this treatment technique is promising, and the development of the structural optimization method to achieve the required structural and functional properties of materials of this class is an urgent and necessary task to be solved.

2. Literature review and problem statement

The microstructure of YSZ–NiO(Ni) cermets for SOFC anodes is formed by processing YSZ–NiO ceramics according to various modes in a high-temperature hydrogen-containing gaseous environment [4, 5]. This allows reducing NiO to Ni and forming an electrically conductive nickel network in the anode [1]. The bearing capacity of SOFC anodes is evaluated by the strength of the materials they are made of [6, 7]. However, the requirements for high porosity of the anodes to ensure the supply of fuel to the zone of its oxidation reaction show that the strength may be an insufficient characteristic of the bearing capacity of the anode. Therefore, more structurally sensitive characteristics are needed to assess its ability to resist the growth of microcracks, which can potentially lead to the failure of the anode and the entire SOFC. All this suggests that it is advisable to study the effect of treatment modes of YSZ–NiO ceramics on its microstructure and propensity to brittle fracture.

Among the mechanical methods of diagnosing the load-bearing capacity of structural ceramic materials and articles made of them, the indentation method is one of the most common and has been used for a long time. Relevant standards [8, 9] regulate the conditions for measuring the microhardness of materials. Vickers microhardness (in GPa) is calculated according to ASTM C 1327 [9] by the formula:

$$HV = 0.0018544\left(\frac{P}{d^2}\right), \quad (1)$$

where P is the load (N), d is the average length of the diagonals of the indentation imprint (mm).

The critical stress intensity factor, K_{Ic}, is another important parameter for the evaluation of fracture toughness of brittle ceramic materials. Methods for estimating fracture toughness of materials under Vickers pyramid indentation have long been proposed. Some of them are thoroughly described and confirmed by experimental data and analytical calculations. A method proposed in the work [6] is one of the first. Based on experimental measurements of force and geometric parameters of indentation of silicon, quartz, silicon carbide, and alumina-based ceramics, the authors proposed the following formulas for estimating fracture toughness of brittle ceramic materials:

$$K_{Ic} = 0.0177\left(\frac{HP}{c}\right)^{1/2},$$

or

$$K_{Ic} = 0.0154\left(\frac{HP}{c}\right)^{1/2}, \quad (2)$$

for silicon carbide and alumina, respectively. These formulas include the following parameters: microhardness H (kgf/mm^2), indentation load P (kg), radial crack length c (mm) according to ASTM C 1327 [5]. K_{Ic} values are obtained in MPa·m$^{1/2}$.

At the same time, based on experimental results obtained during glass indentation, a simplified empirical formula for calculating the critical stress intensity factor K_{Ic} was proposed [11]:

$$K_{Ic} = 0.0726\left(\frac{P}{c^{3/2}}\right). \quad (3)$$

This formula includes only two parameters: the indentation load P (N) and the radial crack length c (m). To obtain the value of K_{Ic} in MPa·m$^{1/2}$, you need to multiply the value obtained by this formula by 10^{-6}.

A similar formula, which differs only in the coefficient (0.0752 vs 0.0726), was proposed in the work [12]:

$$K_{Ic} = 0.0752\left(\frac{P}{c^{3/2}}\right). \quad (4)$$

The same formula, which has a coefficient close to (3) (0.0725 vs 0.0726), was proposed by the authors of the work [13]:

$$K_{Ic} = 0.0725\left(\frac{P}{c^{3/2}}\right). \quad (5)$$

A more complex formula, which has more parameters, was proposed in the works [14, 15] based on empirical results:

$$K_{Ic} = \frac{0.0424(PE/a)^{0.5}}{(c/a)^{1.57}}. \quad (6)$$

This formula includes the following parameters: indentation load P (N), Young's modulus E (GPa), the lengths of the half diagonal of the imprint a (mm) and the radial crack c (mm). K_{Ic} values are obtained in MPa·m$^{1/2}$.

The authors of the work [16], who observed Palmquist-type cracks after indentation with the Vickers pyramid, used this formula to calculate the critical stress intensity factor K_{Ic} in YSZ–NiO ceramics. The authors of the work [17] also used this formula to calculate K_{Ic} in ZrB_2 ceramics after indentation.

Many researchers [18–20] used the formula proposed by the authors of the work [21] for calculating K_{Ic} values:

$$K_{Ic} = 0.016\left(\frac{E}{H}\right)^{1/2}\left(\frac{P}{c^{3/2}}\right). \quad (7)$$

This formula includes the following parameters: Young's modulus E (GPa), microhardness H (GPa), indentation load P (N), and radial crack length c (m). To obtain the value of K_{Ic} in MPa·m$^{1/2}$, you need to multiply the value obtained by this formula by 10^{-6}.

The same formula, which has a coefficient close to (7) (0.014 vs 0.016), was proposed by the authors of the work [22]:

$$K_{Ic} = 0.014\left(\frac{E}{H}\right)^{1/2}\left(\frac{P}{c^{3/2}}\right). \quad (8)$$

The author of the work [23] proposed a more complex empirical formula for calculating the critical stress intensity factor K_{Ic}:

$$K_{Ic} = 0.0285H^{0.6}E^{0.4}a^{0.5}\ln\left(\frac{8.4a}{c}\right). \quad (9)$$

This formula includes the following parameters: microhardness H (MPa), Young's modulus E (MPa), the lengths of the half diagonal of the imprint a (m) and the radial crack c (m). K_{Ic} values are obtained in MPa·m$^{1/2}$.

A similar empirical formula for calculating K_{Ic} was proposed by the author of the work [24]:

$$K_{Ic} = 0.0735H^{0.6}E^{0.4}a^{0.5}\left(\frac{c}{a}\right)^{-0.56}. \quad (10)$$

The units of measurement here are the same as in formula (9).

It should be noted that the invariant values according to formula (2) are obtained only for a narrow range of ceramic materials. Moreover, formula (2) does not take into account the Young's modulus of the material. In formula (6) there is a Young's modulus, but there is no microhardness as a parameter. The same applies to formulas (3), (4), and (5), which do not take into account either the microhardness or the Young's modulus. In formulas (7), (8), (9), and (10) there is a Young's modulus of material and microhardness. Formulas (7) and (8) are similar, but differ by experimentally determined coefficients. The advantage of each of these coefficients should be proved experimentally. In formulas (9) and (10) there are a large number of empirically determined powers for the corresponding material characteristic power functions, and this may limit the use of these formulas. Therefore, it is necessary to check the applicability of all these formulas to determine the fracture toughness of porous cermets.

Based on the study of changes in the microstructure, phase composition, and fracture micromechanism of the YSZ–NiO(Ni) cermet after redox treatment, as well as the values of fracture toughness, it is necessary to assess the propensity of the material to brittle fracture. The performed analysis does not allow to unambiguously choose the optimal formula for calculating the fracture toughness of the studied materials. Each of the above formulas can be used, but there is an issue of reliability of the obtained values. To substantiate and select the most optimal of these formulas for the characterization of the YSZ–NiO anode ceramics and the corresponding cermets, it is advisable to calculate the K_{Ic} value for each of the above formulas for model ZrO_2–Y_2O_3 ceramics. These values should be compared with those obtained for such materials by traditional methods of fracture mechanics.

3. The aim and objectives of the study

The aim of the study was to estimate the effect of redox treatment on the microhardness, fracture toughness, microstructure, and phase composition of the YSZ–NiO(Ni) cermet. This will make it possible to evaluate the crack growth resistance by the Vickers pyramid indentation method and determine the relationship between the fracture toughness and the structural-phase composition of the cermet.

To achieve this goal, the following objectives were set:

– to adapt the Vickers pyramid indentation method for the study of cermet materials;

– to calculate the fracture toughness of the YSZ–NiO(Ni) cermet using the indentation parameters;

– to study the change in the microstructure, fractography and phase composition of the YSZ–NiO(Ni) cermet after redox treatment.

4. Characteristics of the material and features of the research methods used

The ceramics of the YSZ–NiO system, which is perhaps the most common modern material for solid oxide fuel cell anodes, were studied [1, 4].

Plates of YSZ–NiO ceramics (zirconium oxide, stabilized by 8 mol% Y_2O_3, with the addition of 50 wt% NiO; hereinafter – YSZ–NiO) were made by three-dimensional (3D) printing and subsequent sintering. The manufacturing technology of ceramics provided preliminary (700 °C for 2 h) and final (1,450 °C for 2 h) sintering in an argon atmosphere.

The resulting ceramic grain size was 1–2 μm.

Series of prismatic specimens of YSZ–NiO ceramics were undergone to one-time reduction in a hydrogen-containing atmosphere or subjected to reduction-oxidation (redox) cycling at 600 °C (Table 1, [25]). A one-time reduction consisted of heating in vacuum to 600 °C, holding for 4 h in Ar–5 vol% H_2 mixture under a pressure of 0.15 MPa and cooling in argon [2, 3, 26]. Redox treatment was performed for five cycles in a hydrogen-containing medium and air [2, 3, 26]. Specimens were heated in vacuum to 600 °C and held for 4 h in Ar–5 vol% H_2 mixture under a pressure of 0.15 MPa. Next, the chamber was evacuated, the specimens were oxidized in air for 4 h at 600 °C and cooled in air. After redox cycling, the material was reduced in a hydrogen-containing environment and cooled in argon. The heating and cooling rate was 20 °C/min [2, 3].

The fracture stresses for ceramics in the as-sintered state (σ_{f0}) and after treatment (σ_f) were determined from the load–flexure diagrams at 20 °C in air using the appropriate formulas [27, 28]. The relative strength of the material was also determined as the σ_f/σ_{f0} ratio.

The Vickers pyramid indentation technique was adapted to assess the fracture toughness of the ceramic material on model ZrO_2–Y_2O_3 ceramics (zirconium oxide stabilized with 8 mol% Y_2O_3). This ceramic is similar in nature to the YSZ ceramic skeleton in the YSZ–NiO(Ni) cermet structure. Ceramic specimens were made by sintering powders

of zirconium and yttrium oxides in an inert atmosphere at a temperature of 1450 °C. The resulting ceramic grain size was 1–3 μm. The strength and microhardness of ZrO_2–Y_2O_3 ceramics due to the single-phase cubic structure and, accordingly, sintering regimes are 3–7 times higher than those of YSZ–NiO(Ni) cermet [5–7, 16, 29]. Literature sources [30, 31] demonstrate rather invariant results of measured microhardness of such ceramics.

Table 1

Influence of treatment modes on physical and mechanical properties of investigated materials [25]

Variant	Treatment mode	Average value of the characteristics					
		σ_f, MPa	σ_f/σ_{f0}, %	E/E_0, %	E, GPa	σ, S/m	Porosity, %
1	As-sintered material (initial state)	112	100	100	150	(*)	25.2
2	One-time reduction in Ar–5 vol% H_2 mixture	94	84	81.7	123	$2.7 \cdot 10^5$	28.7
3	Redox treatment (5 cycles in Ar–5 vol% H_2 mixture/air) and final reduction in Ar–5 vol% H_2 mixture	108	96	83.1	125	$7 \cdot 10^5$	35.5

Note: (*) The electrical conductivity is very low.

To measure the microhardness of the studied material variants, 6 levels of indentation load were set: 0.49 N, 0.98 N, 1.96 N, 2.94 N, 4.91 N, and 9.81 N. The measurements were performed on a NOVOTEST TC-MKB1 microhardness tester. The method is based on the determination of hardness by the size of the imprint left by the Vickers diamond tip (indenter). The indenter (a diamond regular quadrangular pyramid with an angle at the apex of 136°) is pressed into the surface under the action of a load applied over a period of time [8, 9]. An imprint remains on the surface of the specimen, and the imprint diagonals are used to calculate the arithmetic mean of the length of the diagonal of the imprint. Hardness is calculated as the ratio of the load applied to the indenter to the area of the inclined surface of the imprint. The microhardness tester automatically applies a load to the indenter smoothly, without shocks and vibrations, and provides exposition for 10–15 s. After entering the values of the measured diagonals of the imprint, the microhardness tester automatically calculates the value of the microhardness. The obtained values (in kgf/mm^2) were converted into other units of measurement (GPa) according to ASTM C 1327 [9]. On each variant of the material (Table 1), at least 10 indentations for each of the selected load levels were performed.

Estimation of the fracture toughness of the material under Vickers pyramid indentation was based on the use of an array of force and geometric data. Microhardness, indentation load, and Young's modulus of material were used as force parameters. The geometric parameters of the imprint and crack (if any) were as follows: the length of the indentation diagonal $2a$, the length of the angular crack l, and the total length of the crack c according to ASTM C 1327 [9].

The values of fracture toughness were calculated by formulas (2–10) (section "Literature review and problem statement").

The Young's modulus of YSZ–NiO ceramics in the as-sintered state E=150 GPa was determined based on the analysis of literature sources [6, 7]. We also used our previously proposed method of indirect measurement of the Young's modulus for the material after corresponding treatment [27]. The relative stiffness characteristic E/E_0 was determined (E_0 and E are the values of the Young's modulus for the material in the as-sintered state and after corresponding treatment). Using the slopes of the linear parts of the stress–flexure diagrams, the characteristic E/E_0 was determined as the ratio of the tangents of the slope angles for the material after treatment and in the as-sintered state. To substantiate this approach, we used the formula for the deflection of the beam specimen under the three-point bending [28, 32]

$$\delta = \frac{Ps^3}{48EJ}, \tag{11}$$

where P is the load, s is the span between the supporting rollers, E is the Young's modulus, J is the moment of inertia of the corresponding profile, for a beam of rectangular profile

$$J = \frac{bh^3}{12}, \tag{12}$$

where b is the width and h is the height.

From here, the Young's modulus of the material can be calculated by the formula:

$$E = \frac{Ps^3}{4bh^3\delta}. \tag{13}$$

For some value of δ=const, selected within the elastic section of the stress–flexure diagram, and the same cross-sectional geometry, the following relationship can be written:

$$\frac{E_i}{E_0} = \frac{P_i}{P_0}, \tag{14}$$

or

$$\frac{\sigma_i}{\sigma_0} = \frac{E_i}{E_0}, \tag{15}$$

where E_0 and σ_0 are the Young's modulus and the stress in the material in the as-sintered state, respectively, E_i and σ_i are the Young's modulus and the stress in the material after corresponding treatment, respectively.

Therefore, the modulus E_i can be calculated from the stress–flexure diagram using the formula:

$$E_i = \frac{\sigma_i}{\sigma_0} \cdot E_0. \tag{16}$$

The Young's modulus of YSZ–NiO(Ni) cermets after the corresponding treatments of the as-sintered material (Table 1) was calculated based on the measurements of the corresponding slopes of the stress–flexure diagrams (Fig. 1).

Microstructural and fractographic studies were performed on a Carl Zeiss EVO-40XVP scanning electron microscope (SEM). The elemental composition was determined by local energy dispersive X-ray analysis (EDX) using an INCA ENERGY 350 spectrometer. The geometry of imprints and cracks in the materials was studied using a Neophot-21 optical microscope.

X-ray diffraction studies were performed on a DRON-3.0 diffractometer in monochromatic CuKα radiation.

The porosity of the materials was determined by the hydrostatic weighing method and specified by the express meth-

od of determining the porosity by analyzing their microstructure [33], successfully tested by the authors of the works [34].

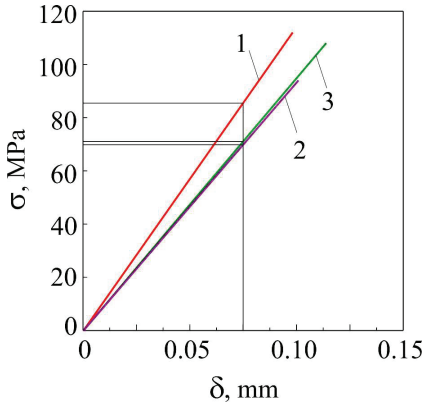

Fig. 1. Stress–flexure diagrams of material of variants 1–3 (Table 1) [25]

5. Estimation of the fracture toughness of materials under Vickers pyramid indentation

To develop a method for estimating the fracture toughness of the material under Vickers pyramid indentation, an array of microhardness data of model ZrO_2–Y_2O_3 ceramics was used. A regression function $H=15.009P^{-0.043}$ was fitted to the data of the obtained experimental dependence of the material microhardness on the indentation load P (Fig. 2, *a*). It satisfactorily describes the relationship between these parameters according to the power law (the coefficient of determination $R^2=0.79$). The regression curve indicates the dependence of the microhardness of the material on the load, known as the indentation size effect in microhardness testing [31, 35, 36], when the average values of microhardness decrease with increasing indentation load.

To calculate the fracture toughness value, a point with a microhardness value H closest to the corresponding position on the regression curve was selected for each indentation load level P. Thus, 6 points were chosen for the indentation load of 0.49 N, 0.98 N, 1.96 N, 2.94 N, 4.91 N, and 9.81 N (points in Fig. 2, *a*, connected by a broken line). The values of the fracture toughness K_{Ic} were calculated by formulas (2–10), using the following material parameters: Young's modulus E (220 GPa [29, 37, 38]); indentation load P; Vickers microhardness H. The geometric parameters of the imprint and crack according to ASTM C 1327 [9] were also used: the length of the indentation diagonal $2a$ and the total crack length c. The dependences of the fracture toughness K_{Ic} of ZrO_2–Y_2O_3 ceramics on the indentation load P obtained by calculating by formulas (2–10) are given in Fig. 2, *b*. There is a tendency to reach the plateau at indentation loads over 4.91 N for the values of fracture toughness, K_{Ic}, calculated by all formulas. The levels of the values of this parameter obtained by different formulas were compared with the values obtained by traditional methods of fracture mechanics [18, 38]. Based on the comparison, it was concluded that formula (7) is the most optimal, because the values of the fracture toughness K_{Ic} obtained by using this formula are closest to those obtained by other methods. The same formula is recommended to be used by other researchers based on the analysis of the obtained calculation results [20, 38, 39].

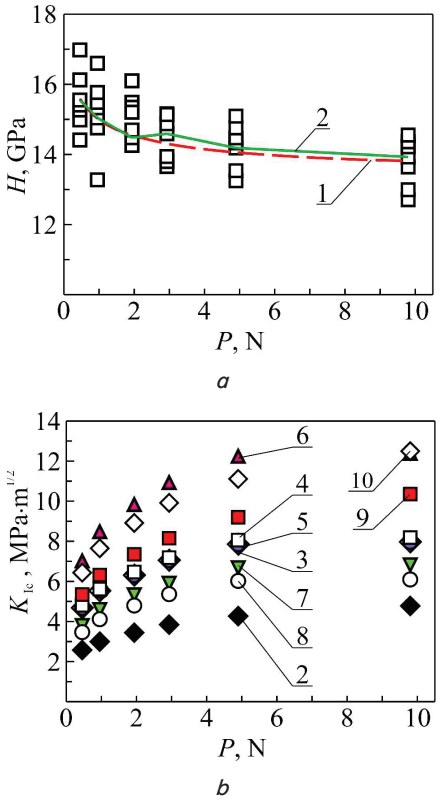

Fig. 2. Change of mechanical characteristics of ZrO_2–Y_2O_3 ceramics under Vickers pyramid indentation conditions depending on the indentation load: *a* – Vickers microhardness (1 – regression function (dashed line); 2 – solid broken line connecting experimental points closest to the corresponding positions on the regression curve); *b* – fracture toughness (the dependence numbers 2–10 correspond to the formula numbers according to which the fracture toughness values, K_{Ic}, were calculated)

The results of microhardness tests of YSZ–NiO ceramics and corresponding cermets (variants 1–3) are presented in Fig. 3 as the dependence of the microhardness of the investigated material variants on the indentation load.

The graph (Fig. 3, *a*) clearly shows the indentation size effect [31]. That is, with increasing indentation load, the average values of microhardness decrease, and the dependence of microhardness on the load reaches the plateau in the range from 2.94 to 9.81 N. In this range, the corresponding average levels of microhardness for materials of variants 1–3 are experimentally determined. For YSZ–NiO ceramics in the as-sintered state (variant 1) this level is 2.0 GPa. For YSZ–NiO(Ni) cermets obtained as a result of both one-time reduction and redox cycling (variants 2 and 3), the level of microhardness is 0.8 GPa.

The values of fracture toughness (in MPa·m$^{1/2}$) of materials of variants 1–3 were calculated by formula (7) for each level of the indentation load P and the obtained value of microhardness H [21].

It was found that the nature of the dependences of the fracture toughness of material variants 1–3 on the indentation load is opposite to that noted for their microhardness. As the indentation load increases, the average values of their fracture toughness increase, and in the range from 4.91 to 9.81 N we observe the plateau-like dependence of their fracture toughness on the load (Fig. 3, *b*). In this range, the

corresponding average levels of fracture toughness were experimentally determined for each of the investigated material variants. For YSZ–NiO ceramics in the as-sintered state (variant 1) this level is 3.75 MPa·m$^{1/2}$, and for cermets (variants 2 and 3) it is 2.9 MPa·m$^{1/2}$. These values are consistent with those obtained for such materials by traditional methods of fracture mechanics [6, 40].

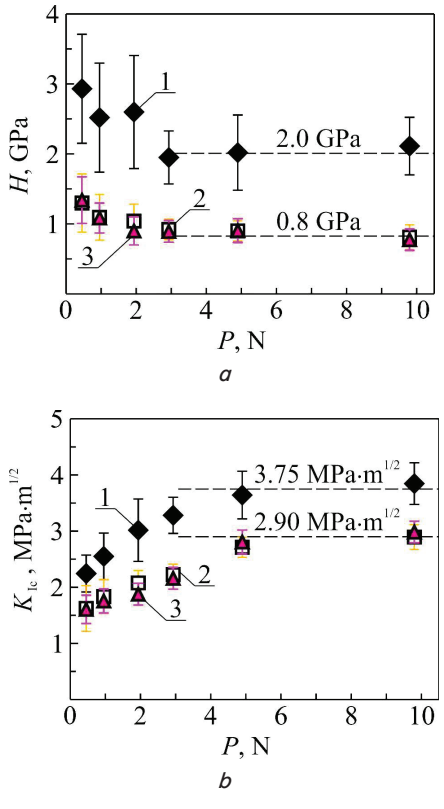

Fig. 3. Change of mechanical characteristics of the investigated materials of variants 1–3 under Vickers pyramid indentation conditions depending on the indentation load: *a* – Vickers microhardness; *b* – fracture toughness. The graphs show the microhardness and fracture toughness values obtained by approximating these parameters to the plateau

6. Analysis of changes in microstructure, microhardness and fracture toughness of YSZ–NiO ceramics due to redox treatment

It is known [3, 25] that the exposure of YSZ–NiO ceramics at a temperature of 600 °C for 4 h in Ar–5 vol % H_2 mixture leads to the formation of thin Ni fringes with a thickness of 0.1–0.3 μm on NiO particles. The residual stresses do not change significantly compared to the as-sintered ceramics, and there are no significant changes in the zirconium phase skeleton. However, due to the partial structural transformation of the nickel phase, a decrease in strength was revealed for this treatment mode (84 % of the value for the as-sintered material [3]). However, nickel fringes united into a network provide satisfactory electrical conductivity of the material.

When YSZ–NiO ceramics were reduced at 600 °C for 4 h in pure hydrogen, nanopores were formed in the particles of the nickel phase due to the rapid shrinkage of the material in a pure hydrogen atmosphere. These nanopores, together with the pores between the particles, prevented the occurrence of residual tensile stresses. However, such a transformation of the nickel phase with a concomitant change in volume and increased porosity caused the loss of a significant number of interparticle bonds. This violated the integrity of the material, leading to a decrease in strength by 48 % of the value for the as-sintered ceramics [3]. Therefore, for a more balanced reduction of the anode material, Ar–5 vol%H_2 mixture was used [25].

For YSZ–NiO ceramics, which was investigated in this work, studies have previously been conducted to determine its strength in the as-sintered state and after the above treatments [25]. We noticed a tendency to a slight decrease in the strength of cermet after one-time reduction (Table 1, variant 2) compared to the as-sintered YSZ–NiO ceramics. After redox cycling, the strength of the cermet remained almost at the same level as for the as-sintered material (Table 1, variant 3). Due to the nickel phase reduction, electrical conductivity of the material of variant 2 increased to a level sufficient for a SOFC anode [1, 26], and electrical conductivity of the material of variant 3 increased significantly compared to that of variant 2 (Table 1, [25]).

The diffraction pattern of ceramics in the as-sintered state (Fig. 4, line 1) contains, in addition to the peaks of the YSZ phase, only peaks that correspond to the NiO phase. The diffraction pattern of the material, one-time reduced in a hydrogen-containing gas mixture (Fig. 4, line 2), contains, in addition to the peaks of the YSZ phase, also peaks that correspond to the NiO and Ni phases. Like the latter, we can see for the material after redox treatment (Fig. 4, line 3) peaks corresponding to all three phases (YSZ, NiO, and Ni). However, we observe slight differences in the shapes of the diffraction patterns of variants 2 and 3, because for variant 3 the peaks corresponding to the Ni phase are slightly higher, and the peaks of the NiO phase are lower than for variant 2.

The analysis of features of microstructure of the reduced cermets of variants 2 and 3 (Figs. 5, *a* and Fig. 5, *b*, respectively) has been carried out. It was found that variant 2 has a relatively homogeneous microstructure with evenly distributed isolated pores (their average size is 2–10 μm). The microstructure of variant 3 is qualitatively different, as we see larger pores (up to 10–20 μm), as well as fragments of the network of combined pores. On the one hand, such structural transformations in the cermet of variant 3 have a positive effect on its functional properties. This is manifested, in particular, in the improved ability to pass the operating environment from the side of its supply to the anode surface in the direction of localization of the oxidation reaction of the fuel at the interface of the anode and electrolyte. On the other hand, this can lead to deterioration of mechanical properties and partial loss of bearing capacity of the anode. The characteristics presented in Table 1 indicate that there was no significant decrease in the strength of the cermet of variant 3 compared to the as-sintered ceramics. On the contrary, we note higher strength compared to one-time reduced material (variant 2).

It should be noted, however, that the gross strength can not fully characterize the bearing capacity of such a highly porous material. More structurally sensitive characteristics are needed to assess its potential ability to resist the initiation and growth of microcracks. Such microcracks can originate from pores both inside (in the bulk) and outside (from the surface and edges) of the anode.

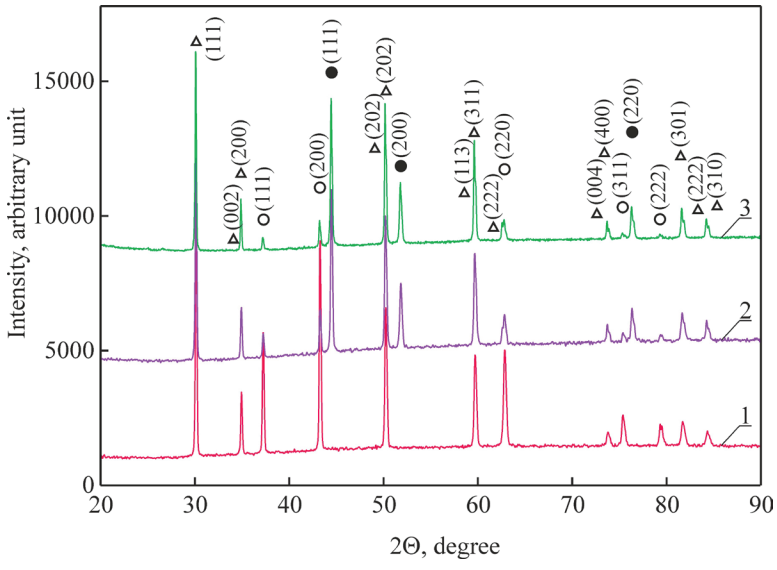

Fig. 4. X-ray diffraction patterns of YSZ–NiO(Ni) anode material: 1 – as-sintered state; 2 – cermet after a one-time reduction; 3 – cermet after redox treatment (Table 1). Light triangles – YSZ phase; light circles – NiO phase; dark circles – Ni phase. The numbers in parentheses indicate the corresponding Miller indices

At high magnifications of the microscope, it was confirmed that variant 2 has a relatively homogeneous microstructure. Light gray areas in Fig. 5, *b*, (zone 1; Table 2, spectrum 1) is a ceramic matrix of zirconium dioxide. In this matrix, the grains of the nickel phase are evenly distributed as dark gray areas separated from each other, each of which is bounded by a white fringe (zone 2 in Fig. 5 *b*; Table 2, spectrum 2). Such dark gray areas are NiO oxide, and white fringes are metallic Ni. The image of the material microstructure of variant 3, made at high magnifications of the microscope (Fig. 5, *d*), shows the result of redox treatment, and one can assess the essence of structural changes in comparison with the material of variant 2. The nickel phase grains (Fig. 5, *d*, zone 4 Table 2, spectrum 4), located in the ceramic matrix of zirconium dioxide (zone 3; Table 2, spectrum 3), generally became smaller. However, the grains contact each other with nickel fringes, forming an electrically conductive network. The smaller ones (0.5–1.5 μm) were completely reduced to metallic nickel, and the larger ones still have a non-reduced core. This explains the 2.6 times higher electrical conductivity of the material of variant 3 compared to variant 2 (Table 1).

The reduction in the nickel phase grain size can be explained by several reasons. First, it is shrinkage, i.e., a significant reduction in the nickel phase volume during the conversion of NiO to Ni [3, 41]:

$$\Delta V_{red} = \frac{V_{\text{Ni}} - V_{\text{NiO}}}{V_{\text{NiO}}} = -41.6\,\%. \qquad (17)$$

Here V_{Ni} is the nickel phase volume after conversion and V_{NiO} is the nickel phase volume before conversion.

Second, it is the diffusion of Ni^{2+} cations in half-cycles of oxidation at 600 °C [4, 42, 43] and, accordingly, the redistribution of nickel in the material bulk.

In the microphotographs of the specimen surfaces with Vickers imprints of materials of variants 1–3 (Fig. 6) at the same indentation load (9.81 N) we observe a difference in their sizes. The diagonals of the imprint on the YSZ–NiO ceramics in the as-sintered state (variant 1) are shorter than on the material of the other two variants. Cracks at the corners of the imprints were fixed for the vast majority of indentations. For example, the enlarged part of the photograph for the material of variant 3 shows a crack from the corner of the imprint length of 12.3 μm (Fig. 6, *c*).

The nature of the initiation and growth of cracks in the reduced cermets depends on the size and morphology of the pores. In the fracture of the specimen of the as-sintered material (Fig. 7, *a*) we observe a smaller number of pores than in the specimens after reduction (Fig. 7, *c*, *e*). Compared to variant 2 (Fig. 7, *c*), slightly larger pores formed in the cermet of variant 3 due to redox cycling (Fig. 7, *e*) serve as potential foci of microcracks.

Table 2

Data of EDX spectra (1–4) of material specimens of variants 2 and 3 (Table 1). The spectra correspond to zones 1–4, indicated by white numbered arrows in Fig. 5

Chemical element	Spectrum 1		Spectrum 2		Spectrum 3		Spectrum 4	
	wt%	at%	wt%	at%	wt%	at%	wt%	at%
O K	19.09	57.30	18.47	49.73	26.03	65.42	12.63	38.06
Ni K	–	–	44.80	32.88	7.86	5.38	53.67	44.08
Y L	6.14	3.32	3.52	1.71	4.99	2.26	2.65	1.43
Zr L	74.77	39.38	33.21	15.68	61.12	26.94	31.06	16.42

At high magnifications of the microscope, multiple facets of transgranular cleavage are observed in the material of variant 1 (Fig. 7, *b*), which indicates the high bond strength between the particles of different phases. This fracture micromechanism corresponds to the relatively high fracture toughness of YSZ–NiO ceramics (Fig. 3, *b*). In the fracture, relatively small pores with a size of 2–5 μm are observed between the agglomerates of sintered ceramic particles (Fig. 7, *b*). These pores do not significantly affect the ceramics fracture toughness. In the material of variant 2, smaller interparticle pores with a size of 0.2–1.5 μm are observed (Fig. 7, *d*), in addition to the observed large pores at small magnifications of the microscope (Fig. 5, *a*). In contrast to this material, even smaller interparticle pores with a size of 0.1–0.3 μm are observed in the cermet of variant 3, and their number is even smaller (Fig. 7, *f*). There are also large pores and their colonies between particle agglomerates of the material (Fig. 5, *c*).

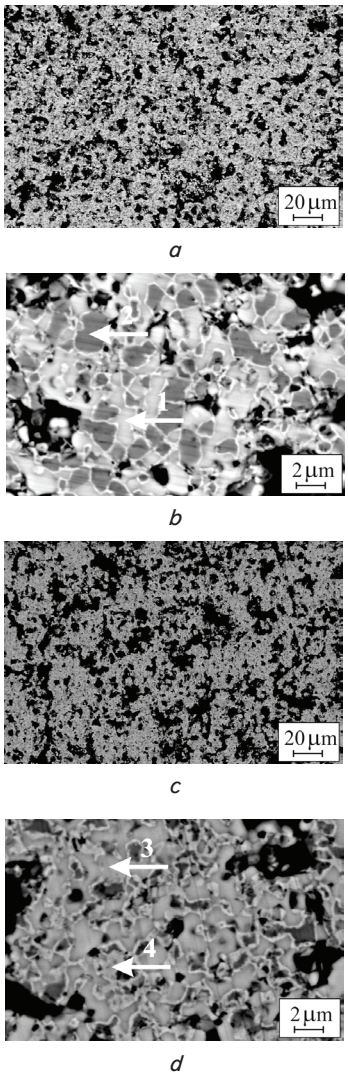

Fig. 5. SEM microstructure of the material: *a*, *b* — variant 2; *c*, *d* — variant 3; *a*, *c* — low magnifications; *b*, *d* — high magnifications. White numbered arrows indicate EDX analysis zones

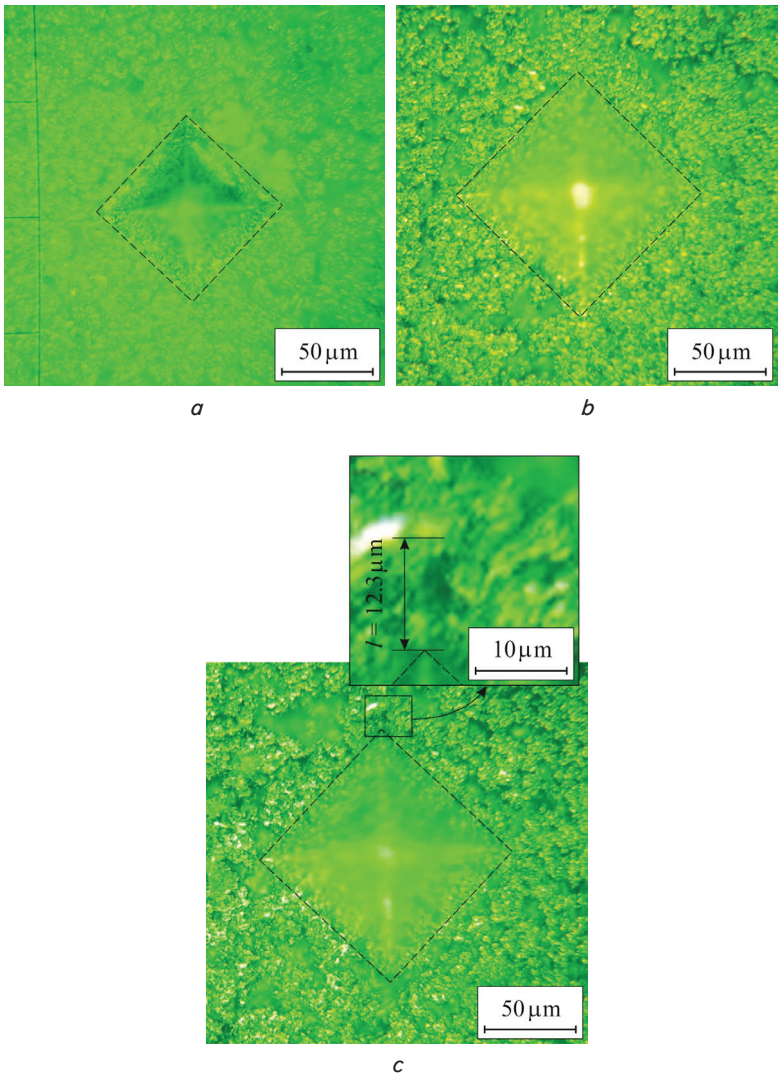

Fig. 6. Optical microphotographs of the specimen surfaces with Vickers imprints obtained under a load of 9.81 N: *a* — variant 1; *b* — variant 2; *c* — variant 3 (the magnified part of the image shows a 12.3 μm long crack started from the corner of the imprint). The contours of the imprints are drawn with dashed lines

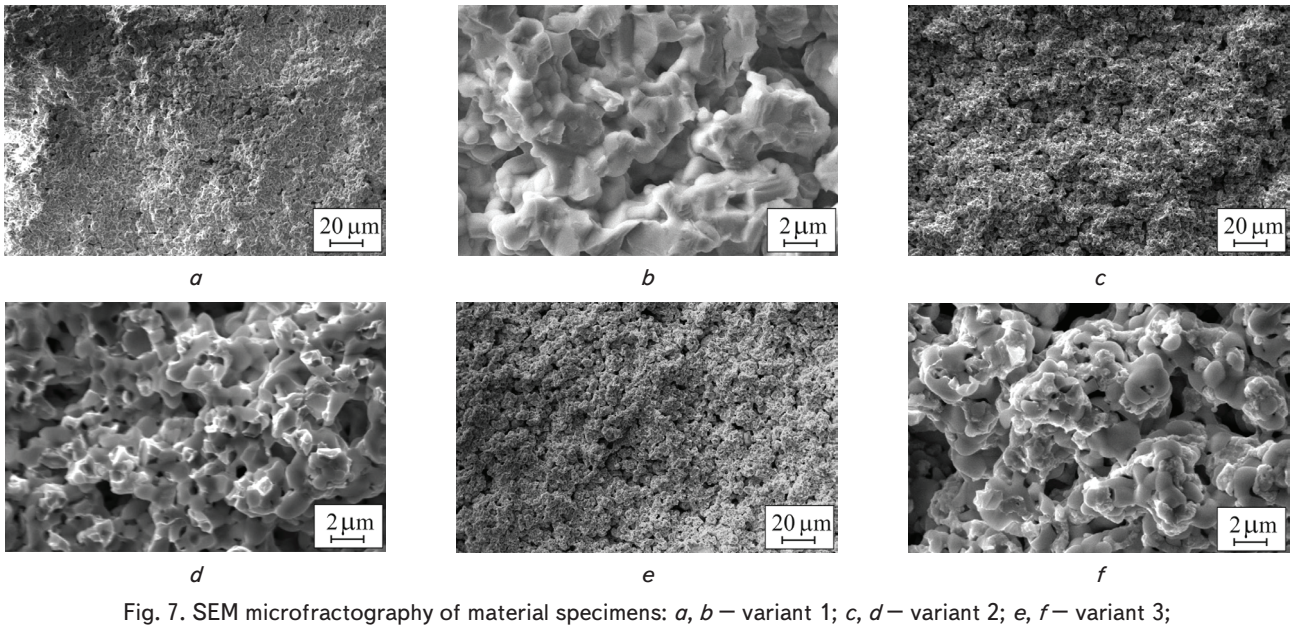

Fig. 7. SEM microfractography of material specimens: *a*, *b* — variant 1; *c*, *d* — variant 2; *e*, *f* — variant 3; *a*, *c*, *e* — low magnifications; *b*, *d*, *f* — high magnifications

7. Discussion of the research results on the estimation of the effect of reduction treatment on the microstructure and crack growth resistance of YSZ–NiO(Ni) materials

The obtained results can be explained by the nature of formation (change) of microstructural components of YSZ–NiO anode ceramics as a result of treatment under different modes in a high-temperature hydrogen-containing gas environment [4, 5]. This treatment provides the reduction of NiO to Ni with the formation of an electrically conductive nickel network (Fig. 5), which serves as a conductor of electrons from the area of the fuel oxidation reaction in a SOFC [1]. Despite the increase in the porosity of the cermet of variant 3 (Table 1), its fracture toughness is not lower than that of variant 2 (Fig. 3, *b*). This can be explained by a detailed analysis of the fracture surfaces. At high magnifications of the microscope, uniformly distributed microregions (up to 1 μm^2) of plastically elongated metallic nickel (Fig. 7, *d*) are observed in the fracture of the material specimen of variant 2. In this case, the intergranular fracture micromechanism, which is characteristic of one-time reduced Ni-containing anode materials, is implemented [1, 7, 16]. For the material of variant 3, we observe a more complex picture. Here, fracture along the boundaries of agglomerates 6–8 μm in size, probably separated by pores, is combined with a small number of microregions of plastically elongated metallic nickel (Fig. 7, *f*). In variant 3, the stresses relax when microcracks reach the particles of the ductile metal nickel phase [4, 41], and the mechanism of "bridging by bonds or fibers" is implemented. This toughening mechanism is known as one of the ways to increase the fracture toughness of brittle materials [44–47]. Therefore, the growing crack bypasses such strengthened agglomerates of particles and propagates along a curved trajectory, uniting relatively large pores, as evidenced by a more relief fracture.

Based on this and previous [2, 3, 25, 43] research, we can conclude that the material reduced by redox treatment has an advantage in strength and electrical conductivity over one-time reduced material. Besides, the material after redox treatment is not inferior to the one-time reduced material in terms of microhardness and fracture toughness. Given these results, the industrial implementation of this treatment at the enterprises for the production of SOFC components looks attractive and promising.

The proposed redox treatment applies only to Ni-containing anode materials, as it is based on the process of nickel phase particle refinement. This refinement occurs due to the cyclic change of the operating environment (reducing/oxidizing) at a temperature of 600 °C. Our studies have shown that the treatment at a temperature of 800 °C does not increase the strength and electrical conductivity of Ni-containing anode materials [25].

Anode materials of other systems, which contain, in particular, oxides of copper and aluminum, are now becoming more and more widely used [48]. Such materials are used in fuel cells running on hydrocarbon fuel. The proposed method for estimating the fracture toughness of material under Vickers pyramid indentation can be effective for characterizing the anode materials of other systems. However, for the application of redox treatment to anode materials of other systems, it is necessary to conduct thorough research that will optimize the modes of this technique. This, in turn, will contribute to the achievement of high electrical conductivity and corrosion resistance, as well as the strength and fracture toughness of the SOFC anodes.

8. Conclusions

1. The method of estimating the fracture toughness of the material under Vickers pyramid indentation conditions based on the analysis of the calculation results using the empirical formulas proposed in the literature has been adapted. The optimal formula is the one that includes the following parameters: Young's modulus, microhardness, indentation load, radial crack length. For the studied cermets, which are characterized by a significant scatter of microhardness values, the optimal range of indentation load was found. In this range, where the microhardness values reach the plateau, the average level of microhardness used to calculate the fracture toughness is determined. The calculated values of fracture toughness are consistent with those obtained by traditional methods of fracture mechanics.

2. The microhardness of YSZ–NiO ceramics and corresponding cermets was measured and the dependences of the microhardness of the investigated material variants and their fracture toughness on the indentation load were constructed. The average levels of microhardness and fracture toughness of the studied materials were determined experimentally. For YSZ–NiO ceramics in the as-sintered state, the microhardness is 2.0 GPa, and for cermets obtained as a result of both one-time reduction and redox cycling, it is 0.8 GPa. The fracture toughness of YSZ–NiO ceramics in the as-sintered state is 3.75 $MPa \cdot m^{1/2}$, and the fracture toughness of cermets is 2.9 $MPa \cdot m^{1/2}$.

3. The influence of one-time reduction in a high-temperature hydrogen-containing gas mixture and redox treatment on the microhardness and fracture toughness of the YSZ–NiO(Ni) cermet was studied and structurally dependent features of its crack growth resistance under Vickers pyramid indentation conditions were determined. Based on microfractographic analysis of the specimen fracture surfaces, it was found that the material after redox treatment exhibits signs of fracture along the boundaries of the agglomerates, separated by pores, and plastic elongation of metallic nickel particles, i.e., the "bridging" mechanism, known as one of the extrinsic toughening mechanisms, is implemented in this material.

References

1. Zhu, W. Z., Deevi, S. C. (2003). A review on the status of anode materials for solid oxide fuel cells. Materials Science and Engineering: A, 362 (1-2), 228–239. doi: https://doi.org/10.1016/s0921-5093(03)00620-8
2. Vasyliv, B. D. (2010). Improvement of the electric conductivity of the material of anode in a fuel cell by the cyclic redox thermal treatment. Materials Science, 46 (2), 260–264. doi: https://doi.org/10.1007/s11003-010-9282-4
3. Podhurska, V., Vasyliv, B. (2012). Influence of NiO reduction on microstructure and properties of porous Ni-ZrO_2 substrates. 2012 IEEE International Conference on Oxide Materials for Electronic Engineering (OMEE), 293–294. doi: https://doi.org/10.1109/omee.2012.6464761

4. Faes, A., Hessler-Wyser, A., Zryd, A., Van herle J. (2012). A Review of RedOx Cycling of Solid Oxide Fuel Cells Anode. Membranes, 2 (3), 585–664. doi: https://doi.org/10.3390/membranes2030585
5. Danilenko, I., Lasko, G., Brykhanova, I., Burkhovetski, V., Ahkhozov, L. (2017). The Peculiarities of Structure Formation and Properties of Zirconia-Based Nanocomposites with Addition of Al_2O_3 and NiO. Nanoscale Research Letters, 12 (1). doi: https://doi.org/10.1186/s11671-017-1901-7
6. Radovic, M., Lara-Curzio, E. (2004). Mechanical properties of tape cast nickel-based anode materials for solid oxide fuel cells before and after reduction in hydrogen. Acta Materialia, 52 (20), 5747–5756. doi: https://doi.org/10.1016/j.actamat.2004.08.023
7. Pihlatie, M., Kaiser, A., Mogensen, M. (2009). Mechanical properties of NiO/Ni–YSZ composites depending on temperature, porosity and redox cycling. Journal of the European Ceramic Society, 29 (9), 1657–1664. doi: https://doi.org/10.1016/j.jeurceramsoc.2008.10.017
8. ASTM E384-11. Standard test method for Knoop and Vickers hardness of materials. ASTM International. doi: http://doi.org/10.1520/E0384-11
9. ASTM C1327-03. Standard test method for Vickers indentation hardness of advanced ceramics. ASTM International. doi: http://doi.org/10.1520/C1327-03
10. Lawn, B. R., Swain, M. V. (1975). Microfracture beneath point indentations in brittle solids. Journal of Materials Science, 10 (1), 113–122. doi: https://doi.org/10.1007/bf00541038
11. Lawn, B. R., Fuller, E. R. (1975). Equilibrium penny-like cracks in indentation fracture. Journal of Materials Science, 10 (12), 2016–2024. doi: https://doi.org/10.1007/bf00557479
12. Evans, A. G., Charles, E. A. (1976). Fracture Toughness Determinations by Indentation. Journal of the American Ceramic Society, 59 (7-8), 371–372. doi: https://doi.org/10.1111/j.1151-2916.1976.tb10991.x
13. Tanaka, K. (1987). Elastic/plastic indentation hardness and indentation fracture toughness: The inclusion core model. Journal of Materials Science, 22 (4), 1501–1508. doi: https://doi.org/10.1007/bf01233154
14. Niihara, K., Morena, R., Hasselman, D. P. H. (1982). Evaluation of KIc of brittle solids by the indentation method with low crack-to-indent ratios. Journal of Materials Science Letters, 1 (1), 13–16. doi: https://doi.org/10.1007/bf00724706
15. Niihara, K. (1983). A fracture mechanics analysis of indentation-induced Palmqvist crack in ceramics. Journal of Materials Science Letters, 2 (5), 221–223. doi: https://doi.org/10.1007/bf00725625
16. Danilenko, I., Glazunov, F., Konstantinova, T., Yashchyshyn, I., Burkhovetski, V., Volkova, G. (2014). Effect Of Ni/NiO Particles On Structure And Crack Propagation In Zirconia Based Composites. Advanced Materials Letters, 5 (8), 465–471. doi: https://doi.org/10.5185/amlett.2014.amwc1040ii
17. Grigoriev, O. N., Vinokurov, V. B., Mosina, T. V., Melakh, L. M., Bega, N. D., Koroteev, A. V. et. al. (2017). Kinetics of Shrinkage, Structurization, and the Mechanical Characteristics of Zirconium Boride Sintered in the Presence of Activating Additives. Powder Metallurgy and Metal Ceramics, 55 (11-12), 676–688. doi: https://doi.org/10.1007/s11106-017-9855-y
18. Gogotsi, G. A., Dub, S. N., Lomonova, E. E., Ozersky, B. I. (1995). Vickers and knoop indentation behaviour of cubic and partially stabilized zirconia crystals. Journal of the European Ceramic Society, 15 (5), 405–413. doi: https://doi.org/10.1016/0955-2219(95)91431-m
19. Ostash, O. P., Kulyk, V. V., Lenkovskiy, T. M., Duriagina, Z. A., Vira, V. V., Tepla, T. L. (2018). Relationships between the fatigue crack growth resistance characteristics of a steel and the tread surface damage of railway wheel. Archives of Materials Science and Engineering, 2 (90), 49–55. doi: https://doi.org/10.5604/01.3001.0012.0662
20. Aswad, M. A. (2014). Comparison of the fracture toughness of high temperature ceramic measured by digital image correlation and indentation method. Journal of University of Babylon, 22 (4), 927–937. Available at: https://www.iasj.net/iasj?func=article&aId=99010
21. Anstis, G. R., Chantikul, P., Lawn, B. R., Marshall, D. B. (1981). A Critical Evaluation of Indentation Techniques for Measuring Fracture Toughness: I, Direct Crack Measurements. Journal of the American Ceramic Society, 64 (9), 533–538. doi: https://doi.org/10.1111/j.1151-2916.1981.tb10320.x
22. Lawn, B. R., Evans, A. G., Marshall, D. B. (1980). Elastic/Plastic Indentation Damage in Ceramics: The Median/Radial Crack System. Journal of the American Ceramic Society, 63 (9-10), 574–581. doi: https://doi.org/10.1111/j.1151-2916.1980.tb10768.x
23. Blendell, J. E. (1979). The Origins of Internal Stresses in Polycrystalline Alumina and Their Effects on Mechanical Properties. MIT Press.
24. Lankford, J. (1982). Indentation microfracture in the Palmqvist crack regime: implications for fracture toughness evaluation by the indentation method. Journal of Materials Science Letters, 1 (11), 493–495. doi: https://doi.org/10.1007/bf00721938
25. Podhurska, V., Vasyliv, B., Ostash, O., Brodnikovskyi, Y., Vasylyev, O. (2016). Influence of Treatment Temperature on Microstructure and Properties of YSZ–NiO Anode Materials. Nanoscale Research Letters, 11 (1). doi: https://doi.org/10.1186/s11671-016-1306-z
26. Waldbillig, D., Wood, A., Ivey, D. G. (2005). Electrochemical and microstructural characterization of the redox tolerance of solid oxide fuel cell anodes. Journal of Power Sources, 145 (2), 206–215. doi: https://doi.org/10.1016/j.jpowsour.2004.12.071
27. Vasyliv, B. D., Podhurska, V. Y., Ostash, O. P., Vira, V. V. (2018). Effect of a Hydrogen Sulfide-Containing Atmosphere on the Physical and Mechanical Properties of Solid Oxide Fuel Cell Materials. Springer Proceedings in Physics, 475–485. doi: https://doi.org/10.1007/978-3-319-92567-7_30
28. Ropyak, L. Ya., Makoviichuk, M. V., Shatskyi, I. P., Pritula, I. M., Gryn, L. O., Belyakovskyi, V. O. (2020). Stressed state of laminated interference-absorption filter under local loading. Functional Materials, 27 (3), 638–642. doi: https://doi.org/10.15407/fm27.03.638

29. Adams, J. W., Ruh, R., Mazdiyasni, K. S. (1997). Young's modulus, flexural strength, and fracture of yttria-stabilized zirconia versus temperature. Journal of the American Ceramic Society, 80 (4), 903–908. doi: https://doi.org/10.1111/j.1151-2916.1997.tb02920.x
30. Lawn, B. (1993). Fracture of Brittle Solids. Cambridge University Press. doi: https://doi.org/10.1017/cbo9780511623127
31. Peng, Z., Gong, J., Miao, H. (2004). On the description of indentation size effect in hardness testing for ceramics: Analysis of the nanoindentation data. Journal of the European Ceramic Society, 24 (8), 2193–2201. doi: https://doi.org/10.1016/s0955-2219(03)00641-1
32. Gere, J. M., Timoshenko, S. P. (1997). Mechanics of Materials. Boston: PWS Publishing Company.
33. Ivasenko, I. B., Posuvailo, V. M., Klapkiv, M. D., Vynar, V. A., Ostap'yuk, S. I. (2009). Express method for determining the presence of defects of the surface of oxide-ceramic coatings. Materials Science, 45 (3), 460–464. doi: https://doi.org/10.1007/s11003-009-9191-6
34. Cherepova, T. S., Dmytrieva, H. P., Dukhota, O. I., Kindrachuk, M. V. (2016). Properties of Nickel Powder Alloys Hardened with Titanium Carbide. Materials Science, 52 (2), 173–179. doi: https://doi.org/10.1007/s11003-016-9940-2
35. Spiridonova, I. M., Sukhovaya, E. V., Pilyaeva, S. B., Bezrukavaya, O. G. (2002). The use of composite coatings during metallurgical equipment parts repair. Metallurgicheskaya i Gornorudnaya Promyshlennost, 3, 58–61. Available at: https://www.scopus.com/record/display.uri?eid=2-s2.0-0036961003&origin=resultslist
36. Ropyak, L. Y., Shatskyi, I. P., Makoviichuk, M. V. (2017). Influence of the Oxide-Layer Thickness on the Ceramic-Aluminium Coating Resistance to Indentation. Metallofizika i noveishie tekhnologii, 39 (4), 517–524. doi: https://doi.org/10.15407/mfint.39.04.0517
37. Shimada, M., Matsushita, K., Kuratani, S., Okamoto, T., Koizumi, M., Tsukuma, K., Tsukidate, T. (1984). Temperature dependence of Young's modulus and internal friction in alumina, silicon nitride, and partially-stabilized zirconia ceramics. Journal of the American Ceramic Society, 67 (2), C-23–C-24. doi: https://doi.org/10.1111/j.1151-2916.1984.tb09612.x
38. Cook, R. F., Pharr, G. M. (1990). Direct Observation and Analysis of Indentation Cracking in Glasses and Ceramics. Journal of the American Ceramic Society, 73 (4), 787–817. doi: https://doi.org/10.1111/j.1151-2916.1990.tb05119.x
39. Nastic, A., Merati, A., Bielawski, M., Bolduc, M., Fakolujo, O., Nganbe, M. (2015). Instrumented and Vickers Indentation for the Characterization of Stiffness, Hardness and Toughness of Zirconia Toughened Al2O3 and SiC Armor. Journal of Materials Science & Technology, 31 (8), 773–783. doi: https://doi.org/10.1016/j.jmst.2015.06.005
40. Khajavi, P., Hendriksen, P. V., Chevalier, J., Gremillard, L., Frandsen, H. L. (2020). Improving the fracture toughness of stabilized zirconia-based solid oxide cells fuel electrode supports: Effects of type and concentration of stabilizer(s). Journal of the European Ceramic Society, 40 (15), 5670–5682. doi: https://doi.org/10.1016/j.jeurceramsoc.2020.05.042
41. Faes, A., Nakajo, A., Hessler-Wyser, A., Dubois, D., Brisse, A., Modena, S., Van herle Jan. (2009). RedOx study of anode-supported solid oxide fuel cell. Journal of Power Sources, 193 (1), 55–64. doi: https://doi.org/10.1016/j.jpowsour.2008.12.118
42. Railsback, J. G., Johnston-Peck, A. C., Wang, J., Tracy, J. B. (2010). Size-Dependent Nanoscale Kirkendall Effect During the Oxidation of Nickel Nanoparticles. ACS Nano, 4 (4), 1913–1920. doi: https://doi.org/10.1021/nn901736y
43. Kharchenko, Y., Blikharskyy, Z., Vira, V., Vasyliv, B., Podhurska, V. (2020). Study of nanostructural changes in a Ni-containing cermet material during reduction and oxidation at 600 °C. Applied Nanoscience, 10 (12), 4535–4543. doi: https://doi.org/10.1007/s13204-020-01391-1
44. Sung Oh, T., Cannon, R. M., Ritchie, R. O. (1987). Subcritical Crack Growth along Ceramic-Metal Interfaces. Journal of the American Ceramic Society, 70 (12), C-352–C-355. doi: https://doi.org/10.1111/j.1151-2916.1987.tb04917.x
45. Sukhova, O. V. (2009). Influence of mechanisms of structure formation of interfaces in composites on their properties. Metallofizika i Noveishie Tekhnologii, 31 (7), 1001–1012. Available at: https://www.scopus.com/record/display.uri?eid=2-s2.0-77952610806&origin=resultslist
46. Ostash, O. P., Anofriev, V. H., Andreiko, I. M., Muradyan, L. A., Kulyk, V. V. (2013). On the concept of selection of steels for high-strength railroad wheels. Materials Science, 48 (6), 697–703. doi: https://doi.org/10.1007/s11003-013-9557-7
47. Ritchie, R. O. (1999). Mechanisms of fatigue-crack propagation in ductile and brittle solids. International Journal of Fracture, 100, 55–83. doi: https://doi.org/10.1023/A:1018655917051
48. Shabri, H. A., Othman, M. H. D., Mohamed, M. A., Kurniawan, T. A., Jamil, S. M. (2021). Recent progress in metal-ceramic anode of solid oxide fuel cell for direct hydrocarbon fuel utilization: A review. Fuel Processing Technology, 212, 106626. doi: https://doi.org/10.1016/j.fuproc.2020.106626